HHS Public Access

Author manuscript

Phys Med Biol. Author manuscript; available in PMC 2018 December 19.

Published in final edited form as:

Phys Med Biol. ; 63(1): 015023. doi:10.1088/1361-6560/aa94bc.

Complex-based OCT angiography algorithm recovers microvascular information superior to amplitude or phase-based algorithm in phase-stable systems

Jingjiang Xu, **Shaozhen Song**, **Yuandong Li**, and **Ruikang Wang***

University of Washington, Department of Bioengineering, Seattle, Washington, USA, 98195

Abstract

Optical coherence tomography angiography (OCTA) is increasingly becoming a popular inspection tool for biomedical imaging applications. By exploring amplitude, phase and complex information available in the OCT signals, numerous algorithms are proposed to contrast functional vessel networks with microcirculation tissue beds. However, it is not clear which algorithm delivers optimal imaging performance. Here, we investigate systematically how the amplitude and phase information would have an impact on the OCTA imaging performance, upon which to establish the relationship of amplitude and phase stability with OCT signal-to-noise ratio (SNR), time interval and particle dynamics. With either the repeated A-scan or repeated B-scan imaging protocols, the amplitude noise increases with the increase of OCT SNR, however the phase noise does the opposite, i.e. it increases with the decrease of OCT SNR. Coupled with experimental measurements, we utilize a simple Monte Carlo (MC) model to simulate the performance of amplitude, phase and complex-based algorithms for OCTA imaging, the results of which suggest that the complex-based algorithms deliver the best performance when the phase noise is < ~40 mrad. We also conduct a series of *in vivo* vascular imaging in animal models and human retina to verify the findings from MC model through assessing the OCTA performance metrics of vessel connectivity, image SNR and contrast to noise ratio. We show that for all the metrics assessed, complex-based algorithm delivers better performance than either the amplitude or phase based algorithms for both the repeated A-scan and B-scan imaging protocols, which agrees well with the conclusion drawn from the MC simulations.

Keywords

optical coherence tomography; optical coherence tomography-based angiography; medical and biological imaging

1 Introduction

As a functional extension to optical coherence tomography (OCT), OCT-based angiography (OCTA) is becoming increasingly important in clinical and pre-clinical applications where it

*Corresponding Author, wangrk@uw.edu.

Disclosures

At the current stage, the authors declare no competing interests in the method discussed in this paper.

is required to image microvascular networks within tissue beds *in vivo*[1–3]. OCTA utilizes the motion of moving particles, e.g. red blood cells (RBCs), as the contrast mechanism to visualize functional blood vessels innervating tissue bed, without a need for exogeneous contrasting agents. Compared to the gold standard fluorescein angiography (FA) and indocyanine green angiography (ICGA) currently used in ophthalmic clinic, OCTA is a label-free, safer, faster and cheaper alternative that can provide more comprehensive information about tissue structure and vasculature in 3D[4]. Recent advances in the development of light source, detection strategy, interferometer design as well as electronics significantly improved the performance of OCT-based angiography. Paralleled with the rapid development of instrumentation, OCTA methods and algorithms also had significant contribution to the high-quality blood flow images obtained in vivo.

In early times, Chen et al. developed phase resolved optical Doppler tomography to measure *in vivo* blood flow by utilizing Doppler frequency shift imparted by moving RBCs in the blood vessels[5]. However, by evaluating the change in OCT signal phases between adjacent A-scans, this method is difficult, if not impossible, to detect slow blood flow within capillary vessels. Wang et al. proposed a novel method named optical angiography (OAG) by using a modified Hilbert transform to convert the modulated OCT signal into complex function, as a consequence, the blood flow signal is efficiently decoupled from static tissue signals[6]. Benefiting from this decoupling, the OAG method images blood vessel networks within tissue beds without contamination from the static tissue background. Due to the increase of OCT imaging speed, novel scanning strategy of repeated B-scans (BM scans) instead of dense A-line scans is evolved, which dramatically improves the flow sensitivity of OCT angiography, enabling the visualization of slow blood flow within capillary tissue beds[7–8]. With the development of bulk motion phase compensation and intensity weighting or thresholding to reduce the phase noise in this scanning mode, the algorithms of phase-variance[9] and Doppler-variance[10] have proposed for OCTA imaging. The method of ultra-high sensitive optical microangiography (OMAG) utilizes the complex information and performs the differential operation (i.e. signal variance) between neighboring B frames for contrasting blood vessels. OMAG has demonstrated capability to resolve capillary-level blood vessels in retina, skin and brain with slow flow velocity down to ~10s μm/s[8], [11–12.] As an adaptive high-pass filter, the approach of eigendecposition- (ED-) based algorithm is developed to efficiently extract the blood flow signals through adaptively rejecting the static tissue components[13–14]. Most of the aforementioned OCTA algorithms are applied in the spectral-domain OCT (SD-OCT) system that has superior stability for both amplitude and phase information.

Recently, the swept-source OCT (SS-OCT) becomes increasingly popular due to its several advantages over SD-OCT, including faster imaging speed, longer imaging range distance, less system sensitivity roll-off along the imaging depth, higher detection efficiency and more compact fiber-based configuration for system design [15]. However, SS-OCT often encounters the problems of severe time jitter and phase instability during cycle-to-cycle sweeping, which would significantly deteriorate the performance of phase-based and complex-based OCTA algorithms. A number of amplitude-based algorithms like speckle variance[16], correlation mapping[17] and split-spectrum amplitude-decorrelation angiography (SSADA)[18] have been proposed to mitigate the strict requirement of high-phase stability. Combined with

amplitude information, the phase gradient method was performed to minimize the trigger-jitter induced phase error and eliminate the bulk phase shift for OCTA imaging in SS-OCT[19]. Several approaches, for example utilizing an additional Mach-Zehnder interferometer[20], external phase reference[21–22] and extra fiber Bragg grating as a fixed wavenumber reference[23] have been proposed to compensate for the time- induced phase error, making it feasible to implement the phase-sensitive angiography algorithms in SS-OCT system. Without the increase of system complexity and computational demand in post-processing, a novel akinetic swept source has been demonstrated to deliver unprecedented phase stability, benefiting the phase- and complex-based OCTA algorithms [24–26].

To date, numerous OCTA algorithms have been reported to provide improved imaging performance in contrasting functional blood vessels, through tackling one or more of following issues: imaging contrast, noise level, motion artifact, hyper-reflection feature, projection (or tailing) artifact and flow sensitivity. These OCTA algorithms can be generally categorized into the following groups: phase-, amplitude- and complex-based algorithms. They may be considered as a family of algorithms, e.g. phase variance, speckle variance and complex variance, which use the same data processing procedures but on different information available in the OCT signals. The ample choice of algorithms often raises confusion about their optimal performance for clinical imaging applications. There are prior investigations attempting to compare different OCTA algorithms, which has helped users understand the strengths and weaknesses of these techniques[27–29]. However, these studies lacked general guidance for algorithm selection for differed imaging applications because they did not systematically investigate how the amplitude and phase information in the OCT signals would have an impact on eventual OCTA imaging performance. In addition, there is also lack of considerations of some practical parameters into the formulation, for example system phase noise level, OCT signal strength as well as motion artifacts.

The Monte Carlo (MC) simulation is a statistical method relying on repeated random sampling of variables from well-defined probability distributions[30]. This approach has been utilized to interpret the light propagation in turbid tissue in OCT studies. Smithies *et al* (1998) introduced an MC model to investigate the influence of multiple scattering effects on signal attenuation and localization in homogeneous samples of intralipid and blood[31]. Yao and Wang also developed a MC model with angle-biased sampling technique to simulate the contribution of the multiple-scattered light in homogeneous turbid media to the OCT signal[32]. In 2002, taking the optical properties of the medium as variables, Wang used the MC simulation to systematically investigated the OCT signal degradation and localization by multiple scattering, and demonstrated how optical clearing could be utilized to enhance the penetration depth and improve the imaging resolution[33]. Since the light interaction between the tissue particles is stochastic in nature and noise is inevitable in the light source and system setup, the amplitude and phase signals become fluctuated in one way or another. In this case, the Monte Carlo (MC) simulation is expected to be an effective method to evaluate the performance of different OCTA algorithms, facilitating its future usage in various pre-clinical and clinical imaging applications.

The purpose of this paper is to provide systematic investigation of the performance of OCTA algorithms utilizing different aspects of OCT information through experimental

measurements and MC simulations. To properly utilize the MC model, we first explore the behavior and stability of amplitude and phase of the OCT signals by experimental measurements of scattering phantoms. The results from these measurements are then fed into a Monte Carlo (MC) model to simulate the performance of amplitude-, phase- and complex-based OCTA algorithms. Finally, *in vivo* OCTA imaging is performed in an animal model and human retina, illustrating the OCTA performance where different algorithms are utilized to contrast the functional blood vessels.

2 System setups and its performance characterization

In this study unless otherwise stated, the experimental work was performed on a home-built fiber-based SD-OCT system because of its high phase stable performance. The schematic of the system is illustrated in Fig. 1, where a broadband superluminescent diode (LS2000C, Thorlabs Inc.) centered at 1340 nm was employed to illuminate the system. The full-wavelength width at half maximum (FWHM) bandwidth of the light source was 110 nm, yielding a high axial resolution of ~7 μm in air. With a 10× scan lens in the sample arm, the transverse resolution was measured at ~10μm, enabling a clear visualization of microvascular networks. A pair of XY galvanometric mirrors (Thorlabs Inc, USA) were used to provide stable scanning patterns for OMAG imaging. The optical power incident on the sample was ~5 mW, leading to an OCT sensitivity of ~105 dB. In the spectrometer, we used an optical grating with a density of 1145 lines/mm and a high-speed line-scan camera (up to 92 kHz) with 1024 pixels, providing an imaging range of ~3 mm with a spectral resolution of ~0.1 nm. A visible red laser (635 nm) was employed in the fiber-based interferometer for the purpose of imaging guidance.

To estimate the stability of the amplitude, phase as well as complex information in the OCT signals, a high reflecting sample (i.e. a mirror) was used as the target in the sample arm, located at the position of ~0.5 mm below zero-delay line. After the captured spectral interferograms were fast Fourier transformed (FFT), a complex matrix containing the OCT amplitude and phase information was created. Fig. 2 results from the consecutive measurements of the target, illustrating amplitude, phase and complex information at the location corresponding to the target. The differential operation between adjacent measurements is similar to a high-pass filtering, which indicates cycle-to-cycle fluctuation in the OCT system. With 92 kHz A-line rate, 4000 consecutive measurements were taken, requiring a total measuring time of ~43.5 ms. During this time-period, the noise of the amplitude (plotted by blue line in Fig. 2(a)) is dominated by high-frequency fluctuation. Removing the DC component of the amplitude, the amplitude difference (plotted by the red line in Fig. 2(a)) demonstrates the instantaneous amplitude stability of the OCT system. Fig. 2(b) is the histogram of the amplitude difference, giving a normal distribution with a standard deviation of 56.3 in arbitrary unit.

The phase is ultra-sensitive to small displacement, and possesses a relationship of $\phi = \frac{4\pi z}{\lambda}$ where ϕ is the phase, z is the optical path length difference, λ is the wavelength of the light source. As shown by the blue curve in Fig. 2(c), the phase has a slow up-and-down shift, most likely due to the low-frequency motion of the target. The value varies from ~ −0.35 rad to 0.02 rad, corresponding to ~34 nm displacement. After filtering out the slow shift of the

target motion, the phase difference between the adjacent measurements is plotted by the red line in Fig. 2(c), which could be used to estimate the instantaneous phase stability of the OCT system.

The corresponding histogram fits well with a normal distribution [Fig. 2(d)]. The standard deviation of the phase difference is ~3.8 mrad, which is sufficiently stable for phase-sensitive OCTA imaging. The corresponding complex numbers (plotted by blue circles in Fig. 2(e)) are scattered in a wide range in the complex plane with an arc shape, mainly due to the bulk motion phase shift of the target. The complex difference values also remove the low-frequency component and are plotted by the red circles in Fig. 2(e). Per the histogram shown in Fig. 2(f), the values of complex differences are closely distributed near the origin point 0, demonstrating a stable performance of both amplitude and phase in the SD-OCT system used in this study.

3. Model characterization

To perform Monte Carlo (MC) simulation for OCTA comparison based on different algorithms, we first developed a simple sample model, where the sample is assumed only containing two homogeneous components, i.e. static particles and moving particles [Fig. 3(a)]. In this paper, the OCT signal-to-noise ratio (SNR) is defined by $SNR_{OCT} = A/\sigma_{noise}$, where A is the OCT magnitude after the FFT of the spectral interferometric signal, σ_{noise} is the standard deviation of noise magnitude[34]. It should be noted that the definition of the OCT SNR might be different from others for the sake of simplifying the expressions of the standard deviation of the amplitude and phase information in this manuscript. Similar to the exponential attenuation of light propagating in the tissue sample, the SNR of OCT signal along the propagating depth also follows Beer–Lambert law:

$$SNR_{OCT}(z) = SNR_{OCT}(0) * \exp(-2\alpha\, z), \quad (1)$$

where z is the optical path length difference with zero delay at the surface of tissue sample, $SNR_{OCT}(0)$ is the initial SNR value at zero position, α is the attenuation coefficient of the sample. As illustrated in Fig. 3(b), the OCT SNR exponentially decreases within tissue sample. We assume that static and moving components have the same attenuation coefficient.

By varying the variable neutral density filter located in the sample arm, we repeated the stability measurements of amplitude and phase with varied OCT SNRs. As shown in Fig. 3(c), the measured standard deviation of amplitude differences increases with the OCT SNR, meaning the stronger of OCT signal results in the more fluctuation of OCT amplitudes. It should be noted that the axis of OCT SNR is in log scale, where the unit of dB is calculated by $20*\log_{10}$ of OCT SNR. The measured data could well fit with an equation of $\sigma_{\Delta A} = 2.46\times10^{-2} * SNR_{OCT} + 51.2$.

Per the experimental data, the standard deviation of amplitude differences is assumed to have a linear relationship with OCT SNR described by:

$$\sigma_{\Delta A,particle}(T,z)=a_{particle}(T)*SNR_{OCT}(z)+b_{particle}(T), \quad (2)$$

where T is the time interval between adjacent measurements. The value of slope $a_{\text{particle}}(T)$ and intercept $b_{\text{particle}}(T)$ are determined by the motion of scattering particles as well as the stability of OCT system during the time of the measurement. Since there are only two types of particles in the model, i.e., static particles and moving particles, the standard deviation of amplitude differences due to static particles could be expressed by $\sigma_{\Delta A,st}(T,z,) = a_{st}(T)*SNR_{OCT}(z) + b_{st}(T)$, while the standard deviation of amplitude differences due to moving particles could be expressed by $\sigma_{\Delta A,fl}(T,z,) = a_{fl}(T)*SNR_{OCT}(z) + b_{fl}(T)$.

On the contrary, the standard deviation of phase differences decreases with the increase of OCT SNR, opposite to that of amplitude statistics. For the phase information, there is a fundamental SNR-limited noise $\sigma_{\Delta\phi,SNR_{OCT}}=1/SNR_{OCT}$ [34], which is plotted by the green line in Fig. 3(d). It should be noted that for the concise equation expression, the OCT SNR definition in this study is slightly different from some other studies in literature. The measured standard deviation of phase differences [blue circles in Fig. 3(d)] is close to the SNR-limited noise. The data could well fit with an equation of $\sigma_{\Delta\phi}=1/SNR_{OCT}+0.34mrad$ [the blue line in Fig. 3(d)], where the 0.34 mrad is the additional phase noise due to slight sample motion or system error. In the MC simulation, we assume that the phase noise terms are uncorrelated, thus the standard deviation of phase differences can be given by:

$$\sigma_{\Delta\phi,particle}(T,z)=\sigma_{\Delta\phi,SNR_{OCT}}(z)+\sigma_{\Delta\phi,particle\ motion}(T)+\sigma_{\Delta\phi,noise}(T), \quad (3)$$

where $\sigma_{\Delta\phi,SNR_{OCT}}(z)=1/SNR_{OCT}(z)$ is the SNR limited phase noise, $\sigma_{\Delta\phi,\ particle\ motion}(T)$ is determined by the internal motion of particles during the time interval, $\sigma_{\Delta\phi,noise}(T)$ is the phase noise including tissue bulk motion, scanning shift, system fluctuation, computation-related error and any other noises. The terms of $\sigma_{\Delta\phi,particle\ motion}(T)$ and $\sigma_{\Delta\phi,\ noise}(T)$ are closely related to the time interval between the adjacent sampling. The static tissue component is assumed to be solid, thus the internal motion contribution of static particles could be neglected. Therefore, the standard deviation of phase differences due to static particles is expressed by $\sigma_{\Delta\phi,st}(Tz,)= \sigma_{\Delta\phi,SNR_{OCT}}(z) + \sigma_{\Delta\phi,noise}(T)$, while the standard deviation of phase differences due to moving particles is given by $\sigma_{\Delta\phi,fl}(T,Z) = \sigma_{\Delta\phi,SNR_{OCT}}(Z) + \sigma_{\Delta\phi,\ fluid\ motion}(T) + \sigma_{\Delta\phi,\text{ noise}}(T)$.

In order to demonstrate and quantify the different behavior for static tissue and moving particles, we constructed a phantom to measure the standard deviation of amplitude differences and phase differences for simulation analysis. In the phantom, a transparent tube with ~400 μm inner diameter was embedded in scattering plasticine, i.e. static tissue component. We used intralipid solution as the moving particles. Here, we diluted the intralipid solution by water with a ratio of 10:90 to attenuate the highly scattering effect. Using a syringe pump, the flow speed was ~1 cm/s, similar to moderate blood flow in real tissue.

Figure 4(a) shows the cross-sectional structure of this phantom. Two different scanning modes, i.e. MB mode and BM mode, were adopted to measure stability of amplitude and phase in different time intervals. The term of MB mode means multiple repeated A-scans are taken at the same transverse location over time and then move to next position to construct a B-frame image. On the other hand, the BM mode refers to multiple repeated B-scans taken at the same B-line position. With 92 kHz A-line rate and 200 Hz B-frame rate, the time intervals between adjacent scans in MB mode and BM mode are ~11 μs and 5 ms, respectively. Fig. 4(b)–(e) show the measured (circles) and fitted (lines) standard deviation of the amplitude differences (middle) and phase differences (right) for the moving particles (top) and static particles (bottom) captured in MB mode (red color) and BM mode (blue color), respectively. For the amplitude information [Fig. 4(b) and (d)], the measured data is well fitted by a linear relationship with OCT SNR in the form of Eq. (2). As for the phase, the measured data is fitted by an inverse relationship with OCT SNR in the form of Eq. (3), except for the moving particles in BM mode. Due to the long-time interval in BM mode, the phase changes due to the moving particles are too large not to have phase wrap, leading to a uniform distribution in the range from $-\pi$ to π. Thus the standard deviation of phase differences is fitted by horizontal line located at ~1.8 rad. The parameter values of the fitted equations are listed in table 1.

4. Monte Carlo simulation method and analyses

To separate the moving component from the static tissue component, we applied an effective algorithm of OMAG[8, 29] as the representative. OMAG performs differential operation between adjacent measurements in the amplitude, phase and complex information:

$$OMAG_{Inf,particle}=\frac{1}{N-1}\sum_{i=1}^{N-1}\left(\left|Inf_{particle,i+1}-Inf_{particle,i}\right|\right), \quad (4)$$

where $Inf_{particle\ i}$, is the information of OCT signal for different particles in the i'th repeated measurement. For example, the amplitude-based OMAG is expressed by $OMAG_{A,fl}=\frac{1}{N-1}\sum_{i=1}^{N-1}(|A_{fl,i+1}-A_{fl,i}|)$, where $A_{fl,i}$ is the amplitude of OCT signal in the i'th repeated measurement. Similarly, the phase- and complex-based OMAG can be written by $OMAG_{\phi,fl}=\frac{1}{N-1}\sum_{i=1}^{N-1}(|\phi_{fl,i+1}-\phi_{fl,i}|)$ and $OMAG_{C,fl}=\frac{1}{N-1}\sum_{i=1}^{N-1}(|C_{fl,i+1}-C_{fl,i}|)$, respectively, where $\phi_{fl,i}$ is the phase information of OCT signal in the i'th repeated measurement, and $C_{fl,i}$ is the corresponding complex information expressed by $C_{fl,i} = A_{fl,i}$ *exp(j$\phi_{fl,i}$) . To evaluate the performance in the simulation model, we define the signal-to-noise ratio of OMAG ($SNR_{OMAG_{Inf}}$) based on different OCT information (amplitude, phase or complex information) by:

$$SNR_{OMAG_{Inf}}=\overline{OMAG_{Inf,fl}}\Big/\overline{OMAG_{Inf,st}}, \quad (5)$$

where $\overline{OMAG_{Inf,fl}}$ is the mean value of *OMAG* based on specified OCT information for all moving particles, $\overline{OMAG_{Inf,st}}$ is the corresponding mean value for all static particles.

According to the phantom experimental data, we make a MC simulation for the two-compartment sample model to investigate how the phase noise affects the performance of OMAG algorithm based on different OCT information. The work flow of the MC simulation is illustrated by Fig. 5(a). To generate the random samplings for OMAG imaging, the mean and standard deviation values of the amplitude and phase information are needed for both static and moving particles. In the MC simulation, we assume the two- compartment sample has an attenuation coefficient of 2.3 mm^{-1} and thickness of 1 mm. With an initial amplitude value of 10^4 at zero depth position and amplitude noise of 30 in arbitrary unit, the OCT SNR ranges from 10 dB to 50 dB within the tissue sample obeying the Beer–Lambert law by Eq. (1). The mean of the phase information (ϕ_0) could be set at any value. We assume that the amplitude and phase have normal distributions with the standard deviations following the relationship described by Eq. (2) and (3). Using the parameter values of MB mode and BM mode in table 1 except for the term of phase noise ($\sigma_{\Delta\phi,noise}(T)$) which we set it as a variable value, we generate 100 million random numbers to simulate the amplitude and phase of 4×10^5 static and moving particles with 5 repeated measurements and 50 variable phase-noise levels at varied depth positions in the sample. Later, according to Eq. (4), we create the OCT angiography for the tissue particles based on the amplitude, phase and complex information. Finally, taking the average of OMAG signal of moving and static particles along the depth direction, the OMAG SNRs based on different OCT information are calculated by Eq. (5).

Figures 5 (b) and 5(c) show the results of OMAG SNR utilizing the amplitude, phase and complex information versus phase noise through the MC simulation. Since the difference of the parameter values between moving particles and static particles increases with the increase of the time interval, the OMAG SNR in the MB mode (as shown in Fig. 5(b)) is relatively low compared to the case of BM mode (Fig. 5(c)). Without the effect from phase noise, the OMAG SNR based on amplitude information maintains at a constant value. In the sample model, the low OCT signals of the static particles in deep region introduce severe SNR-limited phase noise, which results in poor performance for the phase-based OMAG compared to other methods. Utilizing both the amplitude and phase information, the complex-based OMAG works like a balancer (or optimizer) between the methods that use phase and amplitude alone, which greatly reduces the SNR-limited phase noise. Furthermore, the phase fluctuation induced by the moving particles enhances the difference from static particles, which improves the angiography SNR for complex-based OMAG. For both MB and BM scanning modes (shown by Figs. 5(b) and (c)), the complex-based method demonstrates the best angiographic performance when the phase noise is small (less than ~40 mrad). This finding is significant because under the in vivo $\sigma_{\Delta\phi,noise}$ imaging situations, the total phase noise of the whole imaging system is typically ranged from 20 to 40 mrad depending on tissue types, dominated by the cellular movement within in vivo biological tissue. Therefore, we may conclude that complex based algorithms would deliver in vivo imaging performance superior to those algorithms that use amplitude or phase information alone.

5. Imaging results

To verify the MC simulation results, we conducted a series of *in vivo* imaging experiments. Since the time interval of adjacent measurement is an important factor that greatly affects the imaging performance, we adopted two scanning protocols, i.e. MB mode and BM mode, for the visualization of functional blood vessels. We applied a thresholding mask for the OMAG images to avoid phase noise artifact in the non-tissue region. The experimental procedures related to animal imaging were approved by the Institute of Animal care and Use Committee (IACUC) of the University of Washington (Protocol number: 4262-01). The *in vivo* measurements related to human retina imaging were approved by the Institutional Review Board of the University of Washington and informed consent was obtained from volunteer subject before imaging. This study followed the tenets of the Declaration of Helsinki and was conducted in compliance with the Health Insurance Portability and Accountability Act.

For the case of MB scanning mode, we performed the OMAG imaging to visualize the brain blood vessels of a three-month-old mouse (C56/BL6). A technique of thinned-skull cranial window was applied to eliminate the scattering effect from the cranium [35]. During the experiment, the mouse was anesthetized with isoflurane (0.2 L/min oxygen and 0.8 L/min air), and was immobilized on a stereotaxic stage to minimize motion artifacts. For the scanning protocol, the OMAG data contains 200 A positions and 300 B locations with 10 repeated A-scans, which covers the field of view (FOV) of 1.8×2.2 mm^2. As the time interval between adjacent measurements in MB mode is only ~11 μs, the motion contrast to separate the blood vessels from the static tissue has relatively low flow sensitivity (Fig. 6). During this short time interval, the phase noise induced by bulk tissue motion, scanning shift or other errors is also very small (less than 10 mrad).

Since there is ambiguity to identify the blood vessels and static tissues in real OCTA images, it is difficult to evaluate the vascular imaging performance by Eq. (5). To quantify the quality of the vascular images based on different algorithms, we assessed three parameters (i.e. vessel connectivity, image contrast-to-noise ratio (CNR), and image SNR). In doing so, the *en face* images were first normalized from 0 to 1. We applied a threshold at 0.5 to generate binary image to separate the blood vessels from the static tissues. Then the binary image was skeletonized by reducing continuous vessel segments to obtain a vessel skeleton map ($M(x, y)$) with 1 pixel width[36]. In the skeleton map, the vessel connectivity is defined by:

$$Connectivity = \frac{N_{con.}|_{M(x,y)==1}}{N_{tot.}|_{M(x,y)==1}}, \quad (6)$$

where $N_{con.}|_{M(x,y)==1}$ is the number of connected flow pixels and $N_{tot.}|_{M(x,y)==1}$ is the number of total flow pixels. We also defined the image CNR as the following equation:

$$CNR_{IMG}=\frac{\overline{I(x,y)|_{M(x,y)==1}}-\overline{I(x,y)|_{Background}}}{\sigma_{I(x,y)|_{Background}}}. \quad (7)$$

And the image SNR of the angiogram is given by:

$$SNR_{IMG}=\frac{\overline{I(x,y)|_{M(x,y)==1}}}{\sigma_{I(x,y)|_{Background}}}, \quad (8)$$

where $\overline{I(x,y)|_{M(x,y)==1}}$ is the mean value of the strength of *en face* angiogram on the vessel network map, $\overline{I(x,y)|_{Background}}$ is the mean value of the background strength and $\sigma_{I(x,y)|Background}$ is the standard deviation of the background signals. Here, the background area is the non-vascular region where the value is 0 in the binary images. According to the definitions, the parameters of vessel connectivity, image CNR and SNR for Fig. 6(a–c) are tabulated in table 2. Furthermore, with a total of 10 separate experimental measurements on mouse brains using the same system, the averaged values and the standard deviations are also listed and bracketed in table 2.

As illustrated by Fig. 6 and table 2, the OMAG *en face* image based on complex algorithm [Fig. 6(c)] delivers the best vascular visualization in terms of connectivity, CNR and SNR compared to amplitude- [Fig. 6(a)] and phase-based [Fig. 6(b)] algorithms. It can also be observed from the cross-sectional images that the complex-based image [Fig. 6(f)] has the highest blood flow contrast, where the amplitude-based image [Fig. 6(d)] has more noise artifact in the superficial region where there is high OCT SNR, and the phase-based image [Fig. 6(e)] suffers from the SNR-limited noise in the deep region where the OCT SNR is low. The results agreed well with the analyses from MC simulations [Fig. 5(a)].

To investigate the performance in the BM scanning mode, we conducted the *in vivo* OMAG imaging for the ear pinna of a hairless mouse (SKH1, two-month-old). As shown in the cross-sectional structural OCT image [Fig. 7(g)], the ear pinna is a simple tissue model that consists of two layers of skin separated by a cartilage layer. The data contains 400 by 400 transverse positions with 5 repeated B-scans, covering a FOV of 3×3 mm^2. With the frame rate of 200 Hz, the time interval between adjacent B frames is 5 ms, leading to a high-contrast mapping of blood perfusion created by amplitude-based OMAG algorithm [Figs. 7(a) and (d)]. However, the relatively long time interval accumulated severe phase noises that were mainly introduced by mouse breaths, heart beats, stage mechanical vibration or galvo scanning. These phase noises greatly deteriorate the quality of the phase- and complex-based OMAG images [Figs. 7(b)–(c) and 7(e)–(f)].

To minimize the phase noise, we applied a post-processing approach of phase compensation which is based on statistical histogram estimation to correct the phase error of tissue bulk

motion[37]. As a result, the performance of amplitude-based OMAG [Fig. 8(a) and (e)] keeps the same image quality as before; however, there are significant improvements for the phase-based [Figs. 8(b) and (f)] and complex-based [Figs. 8(c) and (g)] OMAG images. In Fig. 8(d), we also generated a histogram of the corrected bulk motion phase in the OMAG images. The standard deviation of the compensated phases is 0.402 rad. After the phase compensation, the complex-based OMAG demonstrates the best imaging performance in terms of vessel connectivity, image CNR and SNR as shown in table 3. Due to the total thickness is only ~ 0.5 mm as observed in the cross-sectional structural image (Fig. 8(h)), the OCT signal of the whole mouse ear pinna is strong. Without severe deterioration of SNR-limited phase noise, the sufficient image quality of phase-based OMAG after phase compensation (Fig. 8(b) and (f)) also result.

Since OCTA has significant clinical value in the field of ophthalmology, we next compared the vascular imaging performance for the algorithms applied to the case of human retina. The data was captured by a commercial SD-OCT system (Zeiss Cirrus HD5000 AngioPlex). The system is equipped with a motion tracking mechanism to minimize the involuntary eye movements, such as microsaccades and drift [38]. To construct the vascular images, there are 245 A-lines along the fast scanning direction and 245 B-scans along the slow scanning direction with 4 repeated B-scans. With 68 kHz A-scan speed, the B-frame rate is 270 Hz, which has a corresponding time interval of ~ 3.7 ms. The scanning FOV is 2.4×2.4 mm^2. Combined with the aforementioned phase compensation approach, we created the OMAG images based on amplitude, phase and complex algorithm. The results are shown in Fig. 9. The cross-sectional structural OCT image (Fig. 9(f)) enables clear visualization of retinal layer (including superficial retina and deep retina), outer nuclear layer (ONL), retinal pigment epithelium (RPE) and choroid. Figs. 9(d)–(f) are the corresponding blood flow images calculated by amplitude, phase and complex-based OMAG algorithms at the position near the fovea. Due to the motion-tracking hardware and software correction of motion artifacts, the complex-based OMAG demonstrates the best blood flow visualization. Utilizing the structural information, a semi-automated segmentation[39] is applied to create the *en face* vascular network of the whole retina as shown in Figs. 9(a)–(c). With additional quantification for these vascular network maps as shown in table 4, the complex-based algorithm delivers the best performance in terms of flow connectivity, CNR and SNR (Table 4). The clear visualization of blood perfusion map in retina is of great importance to diagnose and monitor various eye-related diseases such as glaucoma, diabetic retinopathy and age-related macular degeneration.

6. Discussion and conclusions

As demonstrated in the experimental measurements, the variation of amplitude has an increasing relationship with the increase of the OCT SNR, while the phase information has an intrinsic SNR-limited phase noise that is inversely increased as the decrease of the OCT SNR. Following these measurements, a Monte Carlo (MC) simulation has been used to investigate the OCTA performance of amplitude, phase and complex-based algorithms. It should note that this MC simulation was based on a simplified model where it only contains two homogeneous components, i.e. static and moving particles, with the same attenuation coefficient. These two particles demonstrate different fluctuation behavior in the OCT

amplitude and phase information. In the current simulation, we neglected many factors such as tissue attenuation coefficient variation, multiple scattering, speed of blood flow, concentration of blood cells, tissue complexity, beam size, light focusing and so on, which may also affect the performance of OCTA imaging. The described method of MC simulation would be amendable if it is required to consider these factors into the investigation. Nevertheless, the current MC approach captured the most essential OCTA contrast mechanism, i.e. the dynamic change, to simulate the performance of the algorithms utilizing different parts of OCT signals, which is general enough for clinical OCTA imaging. We have demonstrated that the simulation results agreed well with those from experiments, providing valuable insights as to how the phase noise would affect the OCTA performance. Due to the lack of ability to manipulate the amount of phase noise, the fully validation of the MC simulation is difficult to complete. The work here is the first time to use the MC simulation to estimate the performance of different OCTA algorithms, which should provide a general guidance for selecting appropriate algorithms or optimizing the imaging system.

In this study, we compared the OCTA performance based on different information available in the OCT signal using two scanning modes, i.e. the MB and BM modes. The essential difference between the MB and BM modes is the time interval of the repeated sampling, which influence the measured amplitude and phase variation for the static and moving particles. Typically, in highly stable OCT system (without much noise in the light source and detection), the phase noise induced by sample motion, galvo-scanning and other errors in the MB mode is relatively small due to the short time interval. However, in the BM mode, the relatively long time interval is likely to accumulate the measured phase noise due to inevitable bulk tissue motion. To verify the simulation, we performed the comparison of different algorithms using these two scanning strategies in the animal model and human retinal imaging. For the scenario of MB mode, the complex-based OMAG algorithm demonstrated obvious advantages compared to the amplitude and phase-based algorithms. For the BM scanning mode, the phase noise could be more than 100s mrad due to bulk motion, leading to severe artifacts in the phase and complex-based algorithms. Unless the system is equipped with a motion tracking mechanism, the method of phase compensation can be employed to effectively minimize the phase noise due to tissue bulk motion, which has been demonstrated to greatly improve the image quality of the phase-sensitive OCTA algorithms. In the BM mode after phase compensation, the complex-based OMAG also delivered the best performance. But the superior imaging performance of complex-based OMAG in BM mode is not as impressive as that in the MB mode, which might be due to other time-varying phase noise like tissue morphological change and cellular movement induced phase noises. With flexible scanning strategies, more experiments could be conducted to investigate the influence of different time interval on OCTA imaging.

Currently, there are several OCTA algorithms available in the community, generating questions in terms of their advantages and limitations under different scenarios. We elected to use OMAG algorithm as the representative approach for OCTA imaging, through differential operations on the amplitude, phase and complex information in the OCT signals to contrast functional blood vessels within tissue beds. Other OCTA algorithms could also be investigated by this MC method. With consideration of other factors as well as system parameters, the MC simulation described here would be applicable to commercial or

prototype OCT systems. In the perspective of the SNR of angiographic images, we quantified the OMAG performance based on amplitude, phase and complex information with different phase noises for the cases of the MB and BM scanning modes, where we observed that the complex-based OMAG delivered superior performance in the region of small phase noise (<~0.04 rad). The system stability and signal sensitivity are important factors to consider in order to generate high-quality vascular mapping within tissue beds. In general, the amplitude-based algorithms are relatively immune to the phase stability of the OCT system. For this reason, they have been widely used in swept-source OCT systems that usually have time-jitter induced phase noise. However, the amplitude information is relatively insensitive to motion, and it could be easily affected by tissue hyper-reflection on the surface layer. On the other hand, the phase information is highly sensitive to small displacement at submicron level, which should be in favor for OCT angiography. However, the intrinsic phase-wrap limited by the dynamic range for flow detection, and the inevitable live tissue motion or system mechanical vibration present sources to generate severe phase noises. Furthermore, the phase stability also relies on the strength of OCT signal, giving the SNR-limited phase noise. Therefore, the utilization of the phase information alone in the phase-based OCTA algorithms could be difficult to generate high-quality blood flow images. The complex-based algorithms take the advantages of both the amplitude and phase information to contrast functional blood flow signals within tissue beds. The amplitude strength is used to weigh the phase information, compensating the SNR-limited phase noise. The motion-sensitive phase information further enhances the blood flow signal in OCTA images and reduces the hyper-reflection artifacts. As predicted in the MC simulation, with advanced algorithm or hardware motion tracking mechanism to correct the motion error, the phase noise can be greatly minimized, delivering the best performance for complex-based algorithms.

In future, the rapid development of instrumentation and algorithms would be no doubt to further improve the performance of OCTA imaging. One such improvement would be in the advancement of SS-OCT technology. Recent work has shown that with robust technique of phase stabilization in SS-OCT system, the complex-based OCTA algorithms demonstrated improved vascular image quality and enhanced visualization for the vessels in deep layer[40], which also agrees well with the MC simulation here. It is foreseeable that the further development of the swept light sources and detection strategies will greatly reduce the time-jitter error, providing more and more phase-stable swept-source system for implementing OCTA imaging. With dedicated hardware designs, such as sample fixation and motion tracking as well as sophisticated software controls and algorithms, the tissue motion artifacts are expected to be greatly reduced. Therefore, it is expected that future development of SS-OCT would play a significant role in providing high-quality and high-sensitive functional images of blood vessels within tissue bed.

In summary, we have implemented a highly stable spectral-domain OCT system suitable to demonstrate and investigate the impact of amplitude and phase information on OCTA imaging performances. Using a simple tissue model, we utilized a Monte Carlo simulation for the analysis of OCTA algorithms that use either amplitude, phase or combined information in the OCT signals. The fitted parameters derived from the phantom experiments were fed into the MC simulation, with which to investigate the performance of

amplitude, phase and complex-based algorithms with different phase noise levels in the MB and BM scanning modes. A series of animal experiments as well as clinical OCTA imaging of human retina were conducted to verify the MC simulation. With less phase noise, either due to fast temporal sampling in MB mode or data processing of phase compensation in BM mode, the complex-based algorithm has been demonstrated to deliver the best performance for OCTA imaging. By estimating the system stability and the dynamic status of the static and moving particles, the proposed MC simulation is capable of providing numerical analysis of imaging performance to assess OCTA algorithms, which is helpful in selecting appropriate algorithms for clinical imaging or implementing additional techniques in the system. The purpose of this paper is to serve as a general guidance to choose reliable information with appropriate algorithms in specific applications for OCTA imaging. As the further development of the OCT systems that are of more phase stable, the complex-based algorithms are expected to be the optimal methods for recovering microvascular networks within living tissue beds.

Acknowledgments

This work was supported in part by grants from the National Heart, Lung, and Blood Institute (R01HL093140) and the National Eye Institute (R01EY024158). The content is solely the responsibility of the authors and does not necessarily represent the official views of grant giving bodies.

References

1. Huang D, et al. Optical Coherence Tomography. Science. 1991; 254(5035):1178–1181. [PubMed: 1957169]
2. Kim J, et al. Functional optical coherence tomography: principles and progress. Phys Med Biol. 2015; 60(10):R211–R237. [PubMed: 25951836]
3. Zhang QQ, et al. Wide-field optical coherence tomography based microangiography for retinal imaging. Sci Rep-Uk. 2016; 6
4. de Carlo TE, et al. A review of optical coherence tomography angiography (OCTA). International Journal of Retina and Vitreous. 2015; 1(1):1. [PubMed: 27847594]
5. Chen ZP, et al. Noninvasive imaging of in vivo blood flow velocity using optical Doppler tomography. Opt Lett. 1997; 22(14):1119–1121. [PubMed: 18185770]
6. Wang RK, et al. Three dimensional optical angiography. Opt Express. 2007; 15(7):4083–4097. [PubMed: 19532651]
7. Vakoc BJ, et al. Three-dimensional microscopy of the tumor microenvironment in vivo using optical frequency domain imaging. Nat Med. 2009; 15(10):1219–U1151. [PubMed: 19749772]
8. An L, Qin J, Wang RK. Ultrahigh sensitive optical microangiography for in vivo imaging of microcirculations within human skin tissue beds. Opt Express. 2010; 18(8):8220–8228. [PubMed: 20588668]
9. Fingler J, et al. Volumetric microvascular imaging of human retina using optical coherence tomography with a novel motion contrast technique. Opt Express. 2009; 17(24):22190–22200. [PubMed: 19997465]
10. Yu LF, Chen ZP. Doppler variance imaging for three-dimensional retina and choroid angiography. J Biomed Opt. 2010; 15(1)
11. Xu J, et al. Scalable wide-field optical coherence tomography-based angiography for in vivo imaging applications. Biomed Opt Express. 2016; 7(5):1905–1919. [PubMed: 27231630]
12. An L, Shen TT, Wang RK. Using ultrahigh sensitive optical microangiography to achieve comprehensive depth resolved microvasculature mapping for human retina. J Biomed Opt. 2011; 16(10):106013-106013–106019. [PubMed: 22029360]

13. Yousefi S, Zhi ZW, Wang RKK. Eigendecomposition-Based Clutter Filtering Technique for Optical Microangiography. IEEE Trans Biomed Eng. 2011; 58(8)
14. Zhang Q, Wang J, Wang RK. Highly efficient eigen decomposition based statistical optical microangiography. Quantitative Imaging in Medicine and Surgery. 2016; 6(5):557. [PubMed: 27942476]
15. Song SZ, Xu JJ, Wang RKK. Long-range and wide field of view optical coherence tomography for in vivo 3D imaging of large volume object based on akinetic programmable swept source. Biomed Opt Express. 2016; 7(11):4734–4748. [PubMed: 27896012]
16. Mariampillai A, et al. Speckle variance detection of microvasculature using swept-source optical coherence tomography. Opt Lett. 2008; 33(13):1530–1532. [PubMed: 18594688]
17. Jonathan E, Enfield J, Leahy MJ. Correlation mapping method for generating microcirculation morphology from optical coherence tomography (OCT) intensity images. J Biophotonics. 2011; 4(9):583–587. [PubMed: 21887769]
18. Jia Y, et al. Split-spectrum amplitude-decorrelation angiography with optical coherence tomography. Opt Express. 2012; 20(4):4710–4725. [PubMed: 22418228]
19. Liu GJ, et al. Split-spectrum phase-gradient optical coherence tomography angiography. Biomed Opt Express. 2016; 7(8):2943–2954. [PubMed: 27570689]
20. Braaf B, et al. Phase-stabilized optical frequency domain imaging at 1-mu m for the measurement of blood flow in the human choroid. Opt Express. 2011; 19(21):20886–20903. [PubMed: 21997098]
21. Baumann B, et al. Total retinal blood flow measurement with ultrahigh speed swept source/Fourier domain OCT. Biomed Opt Express. 2011; 2(6):1539–1552. [PubMed: 21698017]
22. Vakoc BJ, et al. Phase-resolved optical frequency domain imaging. Opt Express. 2005; 13(14): 5483–5493. [PubMed: 19498543]
23. Choi W, et al. Phase-sensitive swept-source optical coherence tomography imaging of the human retina with a vertical cavity surface-emitting laser light source. Opt Lett. 2013; 38(3):338–340. [PubMed: 23381430]
24. Bonesi M, et al. Akinetic all-semiconductor programmable swept-source at 1550 nm and 1310 nm with centimeters coherence length. Opt Express. 2014; 22(3):2632–2655. [PubMed: 24663556]
25. Chen Z, et al. Phase-stable swept source OCT angiography in human skin using an akinetic source. Biomed Opt Express. 2016; 7(8):3032–3048. [PubMed: 27570695]
26. Xu J, et al. Wide field and highly sensitive angiography based on optical coherence tomography with akinetic swept source. Biomed Opt Express. 2017; 8(1):420–435. [PubMed: 28101428]
27. Gorczynska I, et al. Comparison of amplitude-decorrelation, speckle-variance and phase-variance OCT angiography methods for imaging the human retina and choroid. Biomed Opt Express. 2016; 7(3):911–942. [PubMed: 27231598]
28. Mahmud MS, et al. Review of speckle and phase variance optical coherence tomography to visualize microvascular networks. J Biomed Opt. 2013; 18(5)
29. Zhang AQ, et al. Methods and algorithms for optical coherence tomography-based angiography: a review and comparison. J Biomed Opt. 2015; 20(10)
30. Wang, L., Jacques, SL. Monte Carlo modeling of light transport in multi-layered tissues in standard C. The University of Texas, MD Anderson Cancer Center; Houston: 1992. p. 4-11.
31. Smithies DJ, et al. Signal attenuation and localization in optical coherence tomography studied by Monte Carlo simulation. Phys Med Biol. 1998; 43(10):3025. [PubMed: 9814533]
32. Yao G, Wang LV. Monte Carlo simulation of an optical coherence tomography signal in homogeneous turbid media. Phys Med Biol. 1999; 44(9):2307. [PubMed: 10495123]
33. Wang RK. Signal degradation by multiple scattering in optical coherence tomography of dense tissue: a Monte Carlo study towards optical clearing of biotissues. Phys Med Biol. 2002; 47(13): 2281. [PubMed: 12164587]
34. Fingler J, et al. Mobility and transverse flow visualization using phase variance contrast with spectral domain optical coherence tomography. Opt Express. 2007; 15(20):12636–12653. [PubMed: 19550532]

35. Li YD, Baran U, Wang RKK. Application of Thinned-Skull Cranial Window to Mouse Cerebral Blood Flow Imaging Using Optical Microangiography. Plos One. 2014; 9(11)
36. Reif R, et al. Quantifying optical microangiography images obtained from a spectral domain optical coherence tomography system. Journal of Biomedical Imaging. 2012; 2012(9)
37. An L, et al. High-resolution wide-field imaging of retinal and choroidal blood perfusion with optical microangiography. J Biomed Opt. 2010; 15(2)
38. Zhang QQ, et al. Wide-field imaging of retinal vasculature using optical coherence tomography-based microangiography provided by motion tracking. J Biomed Opt. 2015; 20(6)
39. Yin X, Chao JR, Wang RKK. User-guided segmentation for volumetric retinal optical coherence tomography images. J Biomed Opt. 2014; 19(8)
40. Song S, et al. Robust numerical phase stabilization for long-range swept-source optical coherence tomography. J Biophotonics. 2017

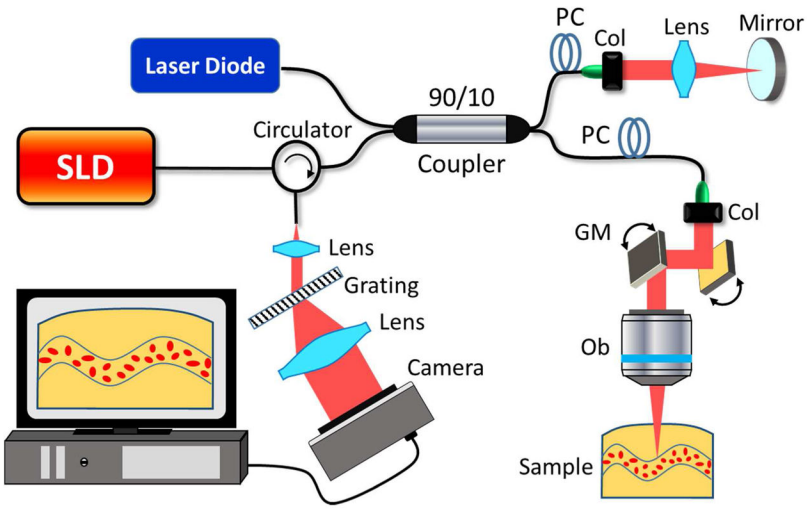

Fig. 1.

Experimental setup of a SD-OCT system. SLD: superluminescent diode, PC: polorization controller, Col: colimator, GM: galvanometric mirrors. Ob: objective lens.

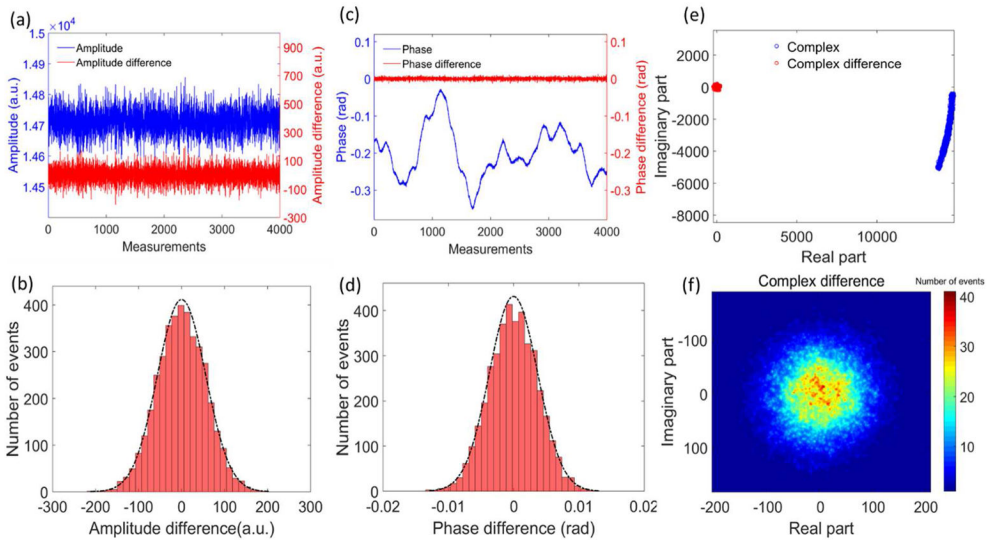

Fig. 2.

The stability assessment for the amplitude, phase and complex information in the SD-OCT system. The top figures (a, c, e) are the consecutive measurements of amplitude, phase and complex information, respectively. The blue plots are the value of amplitude, phase and complex, while the red plots are the difference of amplitude, phase and complex between adjacent A-line scans, respectively. The bottom figures (b, d, f) are the corresponding histograms of the difference values. The black dashed lines in (b) and (d) are the curves of normal distribution fitted from the histograms.

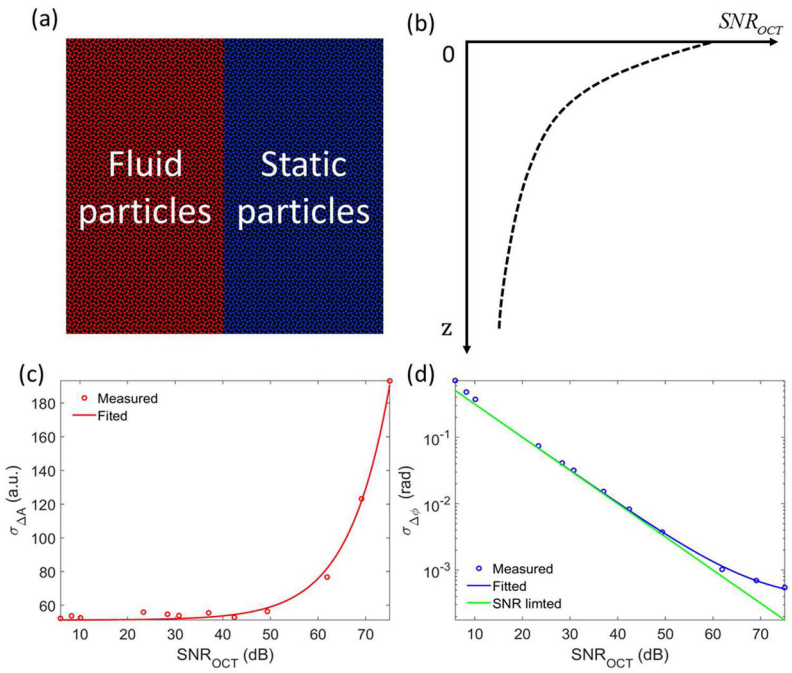

Fig. 3.

(a) Two-compartment simulation model in which only moving and static particles are assumed. (b) The exponential relationship between OCT SNR and the axial depth in the sample. (c) The relationship between the standard deviation of amplitude differences and the OCT SNR. (d) The inverse relationship between the standard deviation of phase differences and the OCT SNR.

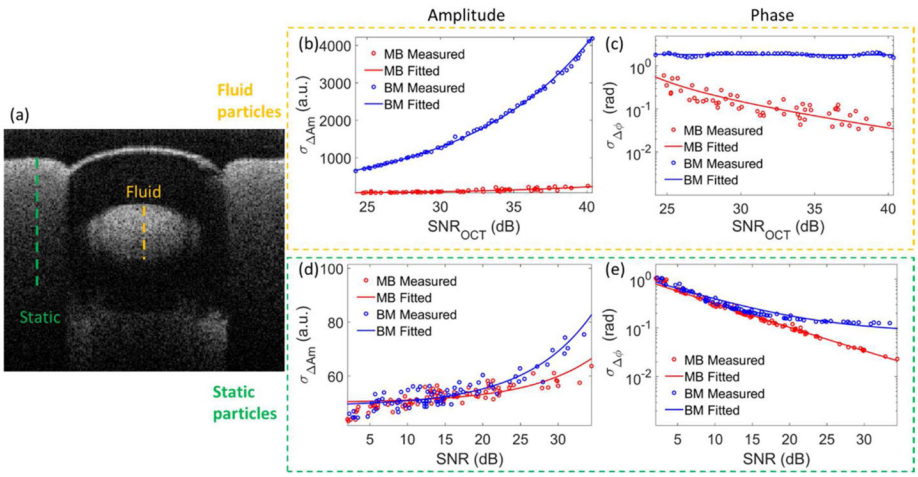

Fig. 4.

The stability assessment of the SD-OCT system when imaging a scattering phantom with intralipid solution being the moving particles. (a) The cross-sectional structural image of the phantom. The measured and fitted plots of the standard deviation of amplitude differences (b) and phase differences (c) versus the OCT SNR in MB mode and BM mode for the moving particles at the position indicated by the orange dashed line in (a). (d) and (e) are the corresponding plots for static particles at the position indicated by the green dashed line in (a), respectively.

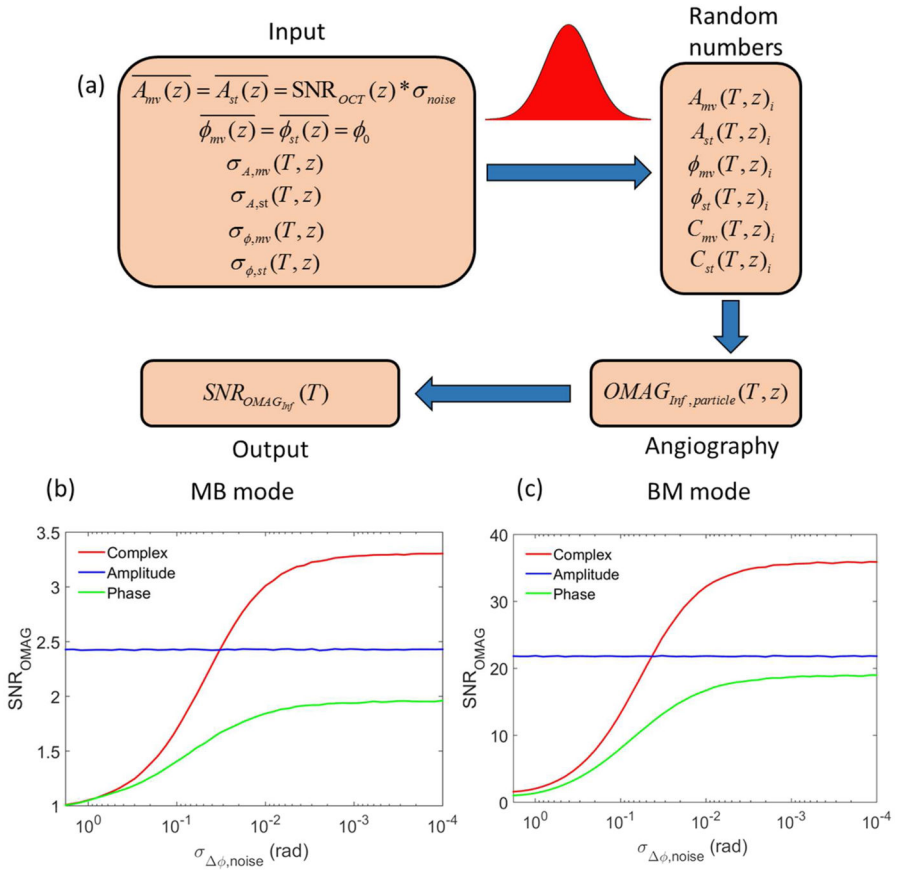

Fig. 5.

(a) The flow chart for Monte Carlo simulation procedure. (b) and (c) are the simulation results of OMAG SNR based on complex (red), amplitude (blue) and phase (green) versus phase noise for MB and BM scanning modes, respectively.

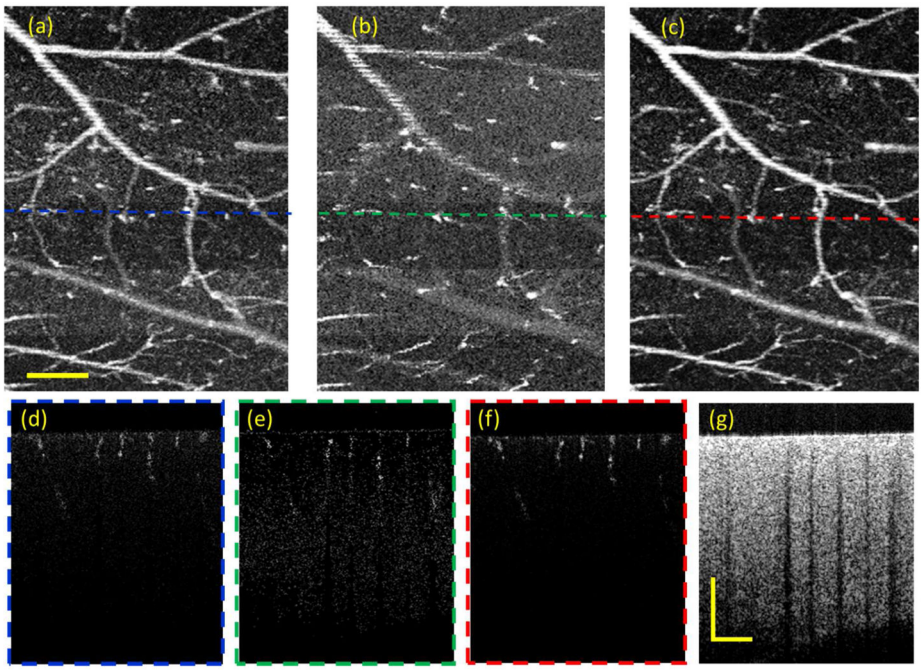

Fig. 6.

OMAG images of mouse brain in MB mode. (a), (b) and (c) are the *en face* MIPs of OMAG based on amplitude, phase and complex information, respectively. (d), (e) and (f) are the corresponding cross-section images at the locations indicated by the dashed lines. (g) is the corresponding structural images. The scale bar = 0.5 mm.

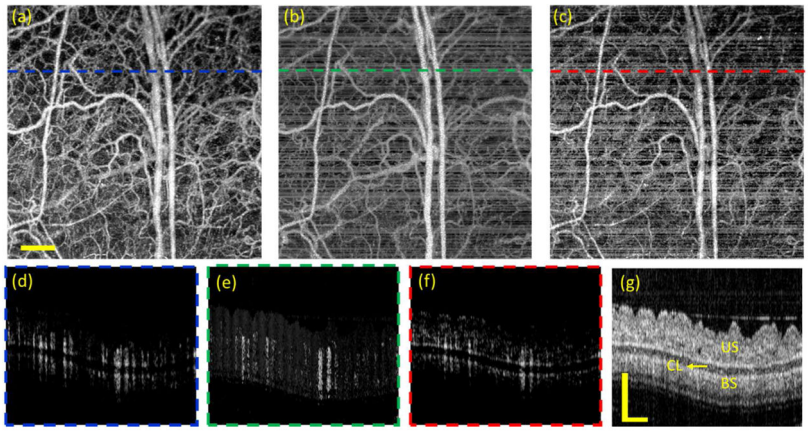

Fig. 7.

OMAG images of mouse ear obtained through BM scanning mode without phase compensation of bulk motion. (a)–(c) are the *en face* blood perfusion maps resulted from amplitude, phase and complex based algorithms, respectively. (d)–(f) are the corresponding cross-sectional blood flow images at the position indicated by the dashed lines in (a)–(c). (g) is the corresponding structural OCT image. CL: cartilage layer, US: upper skin, BS: bottom skin. The scale bar = 0.5 mm.

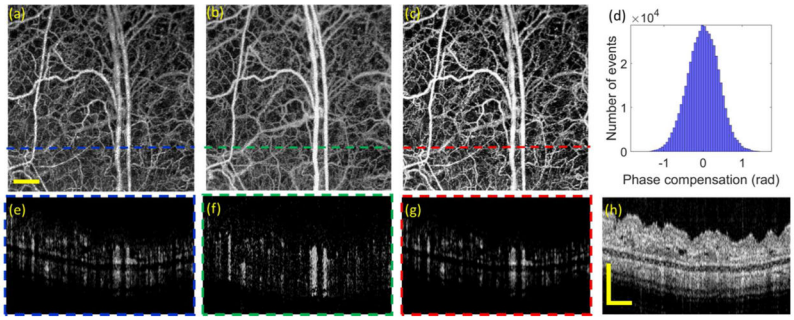

Fig. 8.

OMAG images of mouse ear obtained through BM scanning mode with phase compensation of bulk motion. (a)–(c) are the *en face* blood perfusion maps resulted from amplitude, phase and complex based algorithms, respectively. (e)–(g) are the corresponding cross-sectional blood flow images at the position indicated by the dashed lines in (a)–(c). (h) is the corresponding structural OCT image. (d) is the histogram of phase compensation. The scale bar = 0.5 mm.

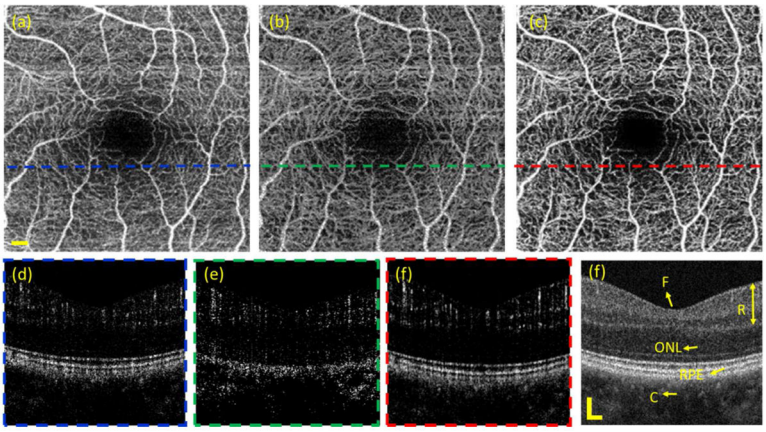

Fig. 9.

OMAG images of human retina obtained through BM scanning mode captured by Zeiss Cirrus 5000 AngioPlex system. (a)–(c) are the *en face* vascular networks of retina resulted from amplitude, phase and complex based algorithms, respectively. (d)–(f) are the corresponding cross-sectional blood flow images at the position indicated by the dashed lines in (a)–(c). (d) is the cross-sectional OCT structural image. F: fovea, R: retinal space, ONL: outer nuclear layer, RPE: retinal pigment epithelium, C: choroid. The scale bar = 0.2 mm.

Table 1

Parameter values of fitted equations.

MB mode	BM mode
$a_{fl}(11\ \mu s) = 1.86$	$a_{fl}(5ms) = 40.46$
$b_{fl}(11\mu s) = 45.36$	$b_{fl}(5ms) = 5.28$
$a_{st}(11\ \mu s) = 0.31$	$a_{st}(5ms) = 0.64$
$b_{st}(11\mu s) = 50.07$	$b_{st}(5ms) = 48.81$
$\sigma_{\Delta\phi,\ fluid\ motion}(11\mu s) = 70mrad$	$\sigma_{\Delta\phi,\ fluid\ motion}(5ms) = 1.8rad$
$\sigma_{\Delta\phi,noise}(11\mu s) = 2.3mrad$	$\sigma_{\Delta\phi,noise}(10\mu s) = 78mrad$

Table 2

The connectivity, CNR and SNR comparisons for mouse brain angiograms in MB mode among three algorithms. The values outside the brackets were resulted from the *en face* images in Fig. 6, while the numbers inside the brackets were the averaged values and the standard deviations calculated from 10 separate experimental measurements.

	Amplitude-based OMAG	Phase-based OMAG	Complex-based OMAG
Connectivity	0.748 (0.711±0.081)	0.546 (0.543±0.052)	0.811 (0.797+0.063)
CNR	4.906 (4.629±0.584)	4.252 (3.543±0.756)	6.084 (5.742±0.414)
SNR	3.759 (3.682±0.281)	2.815 (2.462±0.458)	5.285 (5.045±0.325)

Table 3

The connectivity, CNR and SNR comparisons for mouse ear angiograms in BM mode among three algorithms after phase compensation. The values outside the brackets were resulted from the en face images shown in Fig. 8, while the numbers inside the brackets were the averaged values and the standard deviations calculated from 10 separate experimental measurements.

	Amplitude-based OMAG	Phase-based OMAG	Complex-based OMAG
Connectivity	0.873 (0.851±0.042)	0.835 (0.812±0.074)	0.885 (0.881±0.061)
CNR	3.323 (3.264±0.313)	3.183 (3.105±0.441)	3.857 (3.712±0.395)
SNR	2.548 (2.465±0.217)	2.471 (2.369±0.373)	3.516 (3.502±0.254)

Table 4

The connectivity, CNR and SNR evaluated for human retinal angiograms among three algorithms.

	Amplitude-based OMAG	Phase-based OMAG	Complex-based OMAG
Connectivity	0.909	0.869	0.914
CNR	3.109	2.435	3.528
SNR	2.234	2.178	2.930